



Band Splitting in m-Type II radio Bursts and their Role in Coronal Parameter Diagnostics

Pooja Devi^{a,b,c,*}, Ramesh Chandra^a, Rositsa Miteva^d, M. Syed Ibrahim^e, Kamal Joshi^a

^a*Department of Physics, DSB Campus, Kumaun University, Nainital-263001, India*

^b*Rosseland Centre for Solar Physics, University of Oslo, P.O. Box 1029, Blindern, N-0315 Oslo, Norway*

^c*Institute of Theoretical Astrophysics, University of Oslo, P.O. Box 1029, Blindern, N-0315 Oslo, Norway*

^d*Institute of Astronomy and National Astronomical Observatory - Bulgarian Academy of Sciences, 72 Tsarigradsko Chaussee Blvd., Sofia 1784, Bulgaria*

^e*Department of Physics, Sri Sai Ram Engineering College, Sai Leo Nagar, West Tambaram, Chennai – 600 044 Tamil Nadu, India.*

Abstract

Type II radio bursts are signatures of shock waves generated by solar eruptions, observed at radio wavelengths. While metric (m) type II bursts originate in the lower corona, their longer-wavelength (up to kilometers) counterparts extend into interplanetary space. A rare but valuable feature observed in some type II bursts is band splitting in their dynamic spectra, which provides crucial insights into physical parameters such as shock speed, Alfvén Mach number, Alfvén speed, and coronal magnetic field strength (B). In this study, we investigate band-splitting in 44 m-type II radio bursts observed by the Radio Solar Telescope Network during solar cycle 24 (2009 – 2019). These events exhibit splitting in both fundamental and harmonic bands and are analyzed under both perpendicular and parallel shocks. All events are associated to solar flares and 41 (93 %) with the coronal mass ejections. Shock speeds, derived using a hybrid coronal density model proposed by Vršnak et al. (2004), range from ≈ 350 to 1727 km s $^{-1}$. The relative bandwidth (BDW) of the split bands remains constant with frequency and height. Alfvén Mach numbers indicate moderate shock strength (1.06 – 3.38), while Alfvén speeds and B vary from ≈ 230 – 1294 km s $^{-1}$ and ≈ 0.48 – 7.13 G, respectively. Power-law relationships are established as $BDW \propto f_L^{-0.4}$ and $BDW \propto R^{-1}$, while the coronal magnetic field decreases with height as $B \propto R^{-3}$. These results enhance our understanding of shock dynamics and magnetic field structures in the solar corona.

© 2025 COSPAR. Published by Elsevier Ltd All rights reserved.

Keywords: Type II radio bursts ; Band splitting ; Flares ; Coronal Mass Ejection

1. Introduction

Observations of radio emission from the Sun are most frequently organized in a frequency–time plot, where the intensity was initially ordered as a profile view (de Groot, 1960) but has recently been color-coded. This particular type of plot is termed the dynamic radio spectrum. Its advantages are that low-cost instrumentation could supply high-frequency and high-temporal

resolution data, and a network of similar stations could provide a nearly complete universal time (UT) coverage. The most important disadvantage is the position loss of the radio emission on the solar disk. However, the shapes of the radio features in the dynamic spectrum (historically enumerated from type I to V) point towards the identity and direction of the driver (Warmuth & Mann, 2004). Furthermore, when coupled with a density model, the height over the solar surface of the emitting source could be deduced (Lawrance et al., 2024). Therefore, radio bursts carry rich potential for coronal diagnostics. In this

*Corresponding author:

Email address: setiapooja.ps@gmail.com (Pooja Devi)

study, we focus on the so-called type II bursts.

Solar Type II radio bursts are radio emissions characterized by a slow frequency drift, observable in solar dynamic spectra. The drift rates (rate of change of frequency with time) range from 0.1 to 1 MHz s⁻¹ in the metric (m) domain (upper corona), and decrease to below 0.01 MHz s⁻¹ in the decametric–hectometric (DH) and kilometric domains (interplanetary (IP) space). The m-type II bursts are discovered by Wild & McCready (1950) and have been reported by different research groups (e.g., Ginzburg & Zhelezniakov, 1958; Thejappa & MacDowall, 2000; Gopalswamy et al., 2012a; Frassati et al., 2019; Umuhire et al., 2021; Lawrence et al., 2024; Devi et al., 2024). These bursts often exhibit two distinct components: the fundamental and the harmonic. These correspond to radio emission at the local plasma frequency and twice the plasma frequency, respectively. For a long time, it was believed that type II radio bursts are the signatures of magnetohydrodynamic (MHD) shock waves (Nelson & Melrose, 1985) and can be generated by coronal mass ejections (CMEs), solar flares, and fast plasma flows in regions of reconnection of magnetic field lines (Mann et al., 1995). Further, the onset frequency of Type II radio bursts can serve as a diagnostic for estimating the coronal density at which the CME-driven shock originates. One of the key mechanisms behind the generation of type II solar radio bursts is the Buneman instability (Pikel'Ner & Gintsburg, 1963; Fomichev, 1972; Zaitsev, 1977). This phenomenon arises when a fast-moving shock wave travels through the solar plasma, inducing strong currents. These currents, in turn, lead to the formation of MHD shocks or collective plasma waves in the solar corona and IP space, leading to the generation of observed radio emissions. Recently, Chernov & Fomichev (2021) completed a study on the origin of type II radio bursts. The authors proposed a model to explain these bursts under the framework of the Buneman instability. According to their model, this is fulfilled when two conditions are met: (1) the Alfvén Mach number is higher than a certain limit, and (2) the shock front is nearly perpendicular.

Occasionally, these type II radio bursts show splitting in two

parallel emission bands for a single type II burst in the dynamic spectrum. These splitting can be observed in both the fundamental and harmonic components (Smerd et al., 1974, 1975). In order to explain observed type II band splitting, Smerd et al. (1974) proposed a model according to which the band splitting arises from coherent plasma emission produced in both the upstream and downstream regions of a propagating ahead and behind of the coronal shock wave, respectively. According to this interpretation, the frequency separation between the bands corresponds to the density jump across the shock, with the upstream emission corresponding to the lower-density plasma ahead of the shock and the downstream emission to the denser, compressed plasma behind it. The upstream and downstream are generally denoted by lower frequency branch (LFB) and higher frequency branch (HFB), respectively.

Previously, Mann et al. (1996) studied the 25 m-type II radio bursts observed by Institute for Astrophysics Potsdam spectrograph in 40–170 MHz and calculated the relative instantaneous bandwidth. According to them “*the instantaneous bandwidth of a solar type II radio bursts would reflect the density jump across the associated shock wave*”. Later on, Vršnak et al. (2001) studied the band splitting in coronal and IP type II radio bursts and computed the basic parameters such as: relative band splitting (BDW), and frequency drift, which are important parameters for the estimation of the shock characteristics. Further, Vršnak et al. (2002) and (Vršnak et al., 2004) extended their study of band splitting over 18 m-type II bursts and computed the Alfvén velocity and the coronal magnetic field as a function of the heliocentric distance.

Thus, the most commonly used model to explain the band splitting is by Smerd et al. (1974), as UFB and LFB can be directly used to compute different coronal parameters such as density, Alfvén Mach number, and magnetic field strength (Vršnak et al., 2002; Mahrous et al., 2018; Zucca et al., 2018). After the availability of imaging observations of type II radio bursts this scenario was supported by Zimovets et al. (2012); Zucca et al. (2014); Chrysaphi et al. (2018), for selected case studies. On the other hand, alternative models exist to explain the

band-splitting due to two different radio sources at two different locations in the upstream of the shock front (Zaitsev, 1978; Holman & Pesses, 1983). Recently, Normo et al. (2025) studied the event of band splitting with LOFAR data on 23 May 2022 and found that both bands originate in two separate upstream regions. Despite the alternative theories, we decided to adopt the one by Smerd et al. (1974) in our study mostly due to its straight-forward deduction of physical parameters and the lack of imaging data for our entire event list.

In this study we adopt the premise that the frequency separation between the split bands provides an estimate of the density compression ratio across the shock. This allows inferring the shock parameters such as: the Mach number and finally the coronal magnetic field strength, which are difficult to measure directly. Since the band splitting is more clearly visible in the m-region (~ 300 MHz frequency band), in this paper, we present the m-type II radio bursts with band splitting and their relationship with various flare, CME, and other coronal parameters (such as Alfvén Mach number, height of shock formation, and coronal magnetic field strength). Section 2 describes in details the data sets and the selection criteria. The subsequent parts are devoted to the obtained results (Section 3) and their discussion (Section 4). Finally, the summary of the study is structured in Section 5.

2. Data Sets

In this study, we used data from the Radio Solar Telescope Network (RSTN) which covers the radio spectrum in the frequency range $25 - 180$ MHz with its four stations, namely Learmonth Hill, San Vito, Palehua, and Sagamore Hill, covering the full day observations. We started from the type II radio burst catalog as compiled by Lawrance et al. (2024) and Devi et al. (2024). From their list, we selected the events that show clear band splitting in both fundamental and harmonic bands. Note that the frequency ratio of these splitted bands are different from $\frac{f_{\text{harmonic}}}{f_{\text{fundamental}}} = 2$ (nearly) as defined in Vršnak et al. (2001), which means that they are different from what are called as “fundamental” and “harmonic” bands. Of the 429 m-

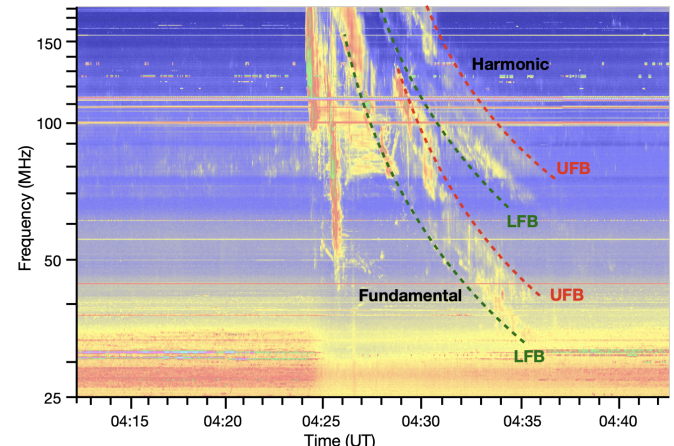


Fig. 1. An example of m-type II radio burst from Learmonth Hill on 08 November 2013 showing the fundamental and harmonic bands. The UFBs and LFBs are shown with red and green dashed curves, respectively.

type II radio bursts observed by RSTN during solar cycle 24 in the list of Lawrance et al. (2024), we found clear band splitting in 44 events. An example of band splitting in the fundamental and harmonic bands on 08 November 2013 from the Learmonth Hill station is shown in Figure 1. The figure clearly show the UFB and LFB in both fundamental and harmonic bands.

After the selection of events, we checked their association with the solar flares, CMEs, and the DH type II radio bursts. The information about flares is taken from the NOAA solar region summary reports (solar_region_summary_reports), CMEs from the LASCO CME catalog (Gopalswamy et al., 2009, https://cdaw.gsfc.nasa.gov/CME_list/), and of the DH type II bursts from the Wind/WAVES type II catalog (Gopalswamy et al., 2019, https://cdaw.gsfc.nasa.gov/CME_list/radio/waves_type2.html). We found that all the events are associated with solar flares and 41 (93 %) are associated with CMEs. Out of 44 m-type IIs, 12 events (i.e., $\approx 27\%$) are associated with the DH-type II radio bursts. Out of these 12 DH-type IIs, eight (i.e., $\approx 67\%$) are associated with halo CMEs. A table containing the parameters of these band-split m-type IIs and their associated flares, CMEs, and DH type IIs, is presented in the Appendix as Table A.1. The description about the associated flares, CMEs, and various parameters computed from these band-split m-type II bursts are provided in the following Section.

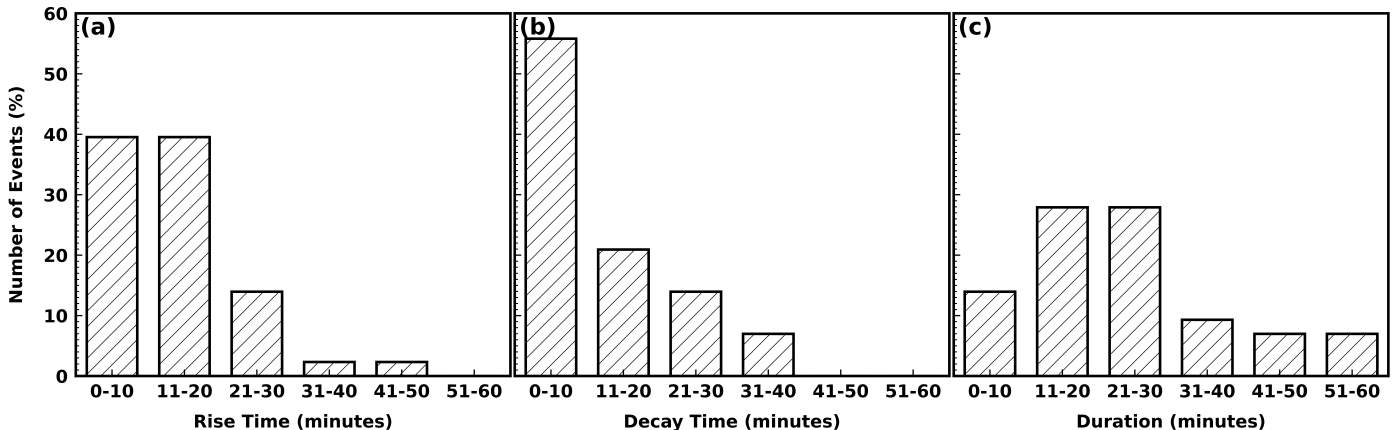


Fig. 2. m-type II radio bursts associated flare parameters namely rise time, decay time, and duration of flares in panels (a), (b), and (c), respectively.

3. Results

3.1. Relationship with flares

We cross-checked the relationship of the type IIs in this study with the flares and CMEs. We found that all of these type IIs are associated with moderate to strong flares, as can be seen in Table A.1. Among these flares, one ($\approx 2.3\%$) is B-class, 12 ($\approx 27.3\%$) are C-class, 24 ($\approx 54.5\%$) are M-class, and six ($\approx 13.6\%$) are X-class flares. The remaining one event is associated with a strong flare (observed by the Solar TErestrial RElations Observatory) but it is located behind the limb, when viewed from Earth. Thus, there is no GOES class for this event. The plots of flare rise time, decay time, and flare duration versus number of events are presented in panels (a), (b), and (c) of Figure 2, respectively. The rise time, decay time, and duration of the flare are calculated as the difference between start and peak times, peak and end times, and start and end times, respectively. From the figure, we see that the majority of the flares ($\approx 80\%$) are impulsive in nature, i.e., their rise time is within 20 minutes. Also, many events ($\approx 57\%$) have a decay time within 10 minutes. In case of the duration of these flares, $\approx 12\%$ of which are within 10 minutes, $\approx 58\%$ are within 11 – 30 minutes and rest are in 31 – 60 minutes time range, respectively.

Next, we find the source of the m-type II radio bursts on the solar disk by investigating the location of associated flares. The distribution of the source latitudes and longitudes are shown in Figure 3. From the figure, we see that the type II bursts occur

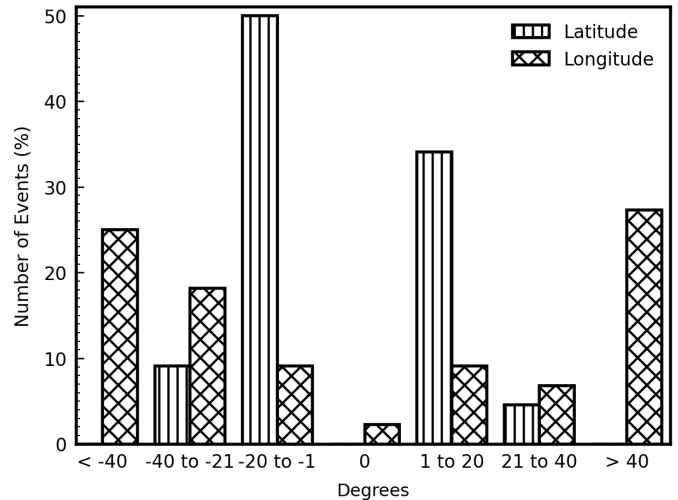


Fig. 3. Distribution of location of the sources of m-type II radio bursts on the solar disk. The bars with “vertical lines” and “crosses” represent the latitude and longitude of the source location, respectively.

within the latitude of $\pm 30^\circ$, whereas they originate from all the longitudes that cover from 0° to $\pm 90^\circ$. Many events ($\approx 51\%$) lie in the bin of -1° to -20° latitude and reach maximum up to -24° latitude (where the negative sign is selected to denote Southern latitudes in the plots). After careful examination of the events, we find that 26 events, i.e., 59 %, have their source located in the Southern hemisphere and the remaining 17, i.e., $\approx 39\%$, originate from the Northern hemisphere. In one case, we could not find the location on the disk, because of a back-side event (behind the limb). For the case of helio-longitudes, 23 events ($\approx 52\%$) are from the Eastern and 19 ($\approx 43\%$) are from the western hemisphere. The remaining one event has its source at 0° longitude. The source locations on the solar disk

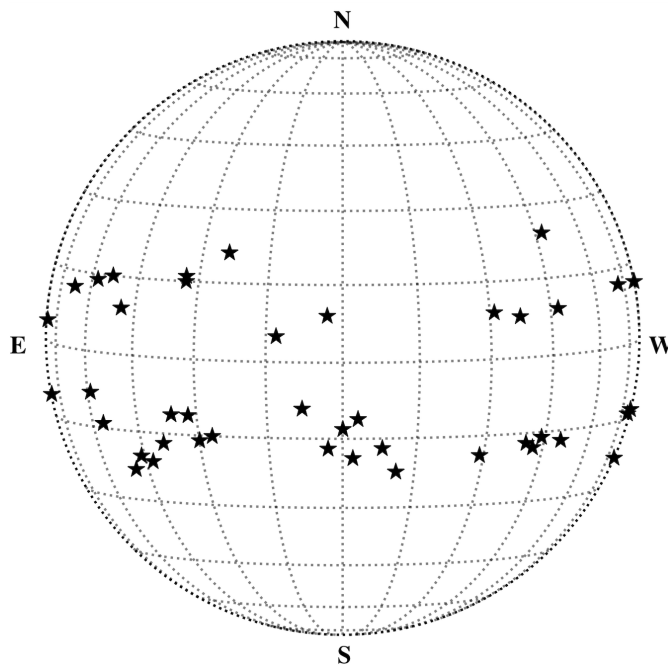


Fig. 4. Locations of m-type II burst sources shown on the solar disk with star symbols.

are visualized in Figure 4 with star symbols.

3.2. Relationship with CMEs

In order to identify the relationship of these m-type IIs with CME, we used data from the LASCO CME catalog. From there, we found that 41/44, i.e., $\approx 93\%$ of these m-type IIs are associated with CMEs. The remaining three events are: (1) event no. 12 was originated on 25 September 2012 and was associated with a weak flare of GOES C3.6 class. (2) The event no. 20 on 25 October 2013 was associated with a failed eruption accompanied by an EUV wave, and a jet from the flaring active region. (3) The event no. 28 originated on 22 August 2014 was associated with a very weak flare of GOES B-class and a jet activity.

From the LASCO CME catalog we take parameters such as speed, acceleration, and angular width. Their histograms are presented in Figure 5, panels (a), (b), and (c), respectively. From all events, $\approx 39\%$ have CME speeds in the range $201 - 400 \text{ km s}^{-1}$, and about 10 % of CMEs have a very high speed, that is, $> 1000 \text{ km s}^{-1}$. Panel (b) of the figure shows that a large fraction of the CMEs ($\approx 57\%$) are decelerated up to 20 m s^{-2} . However, all CMEs have an acceleration ranging from -60

to more than 20 m s^{-2} . The angular width of these CMEs (Figure 5(c)) confirms that $\approx 27\%$ (12/44) of the events are halo. A similar number of events lie in the ranges of $81^\circ - 120^\circ$ and $121^\circ - 359^\circ$.

3.3. Coronal and shock parameters

Several key parameters of the coronal plasma and the shock wave are calculated on the basis of our event selection. The description of these parameters are given in the following subsections.

3.3.1. Density

The density is directly related to the frequency with the following expression,

$$f[\text{MHz}] = 9 \times 10^{-3} \times \sqrt{n}; \quad (1)$$

$$n[10^{-8} \text{ cm}^{-3}] = \left(\frac{f}{9 \times 10^{-3}} \right)^2$$

Figure 6 shows the histogram of the density calculated from the fundamental and harmonic bands using equation 1. The averaged density derived from the fundamental bands is higher (up to $1.9 \times 10^8 \text{ cm}^{-3}$) than that of the harmonic bands (maximum $0.75 \times 10^8 \text{ cm}^{-3}$). In case of the density computed from fundamental bands, the distribution of events in the different density ranges is as follows:

- $\approx 39\%$ in $0 - 0.3 \times 10^8 \text{ cm}^{-3}$
- $\approx 25\%$ in $0.31 \times 10^8 - 0.6 \times 10^8 \text{ cm}^{-3}$
- $\approx 27\%$ in $0.61 \times 10^8 - 0.9 \times 10^8 \text{ cm}^{-3}$
- $\approx 9\%$ in $0.91 \times 10^8 - 2 \times 10^8 \text{ cm}^{-3}$.

However, in case of the harmonic bands, nearly equal numbers of events can be found in two density bins, namely:

- $\approx 38\%$ in $0 - 0.3 \times 10^8 \text{ cm}^{-3}$
- $\approx 38\%$ in $0.31 \times 10^8 - 0.6 \times 10^8 \text{ cm}^{-3}$
- $\approx 24\%$ in $0.61 \times 10^8 - 0.9 \times 10^8 \text{ cm}^{-3}$.

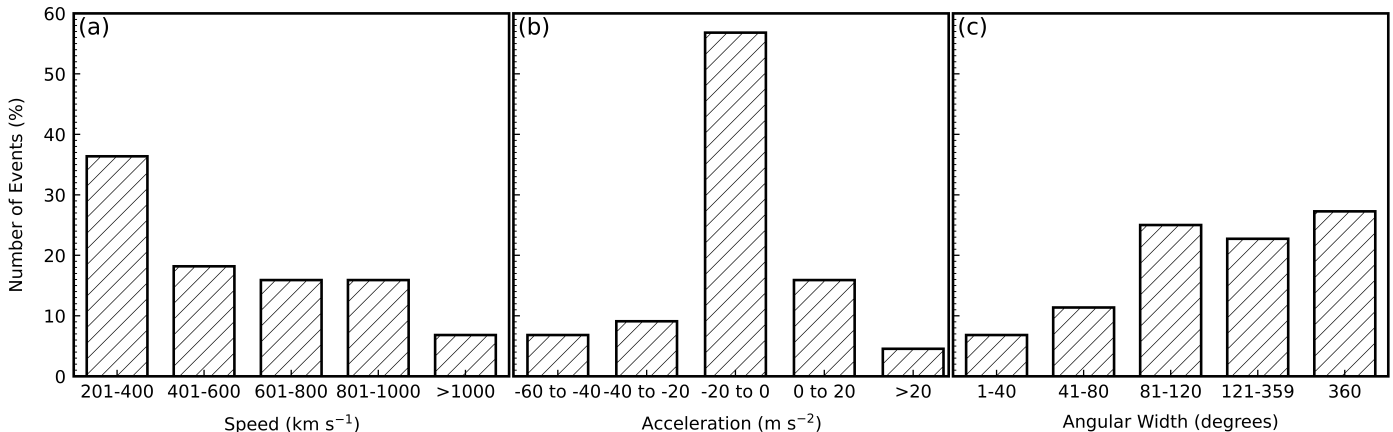


Fig. 5. Histograms of speed, acceleration, and angular width of the CMEs associated with m-type II radio bursts.

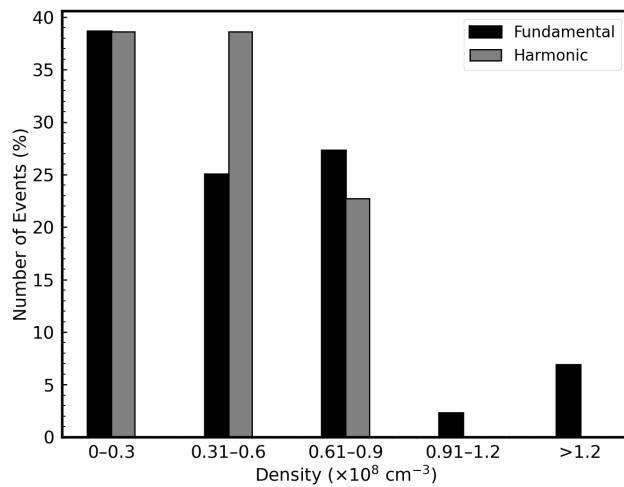


Fig. 6. Histogram of density with number of events. The densities computed using the fundamental and harmonic bands are plotted with black and gray colors, respectively.

3.3.2. Type II speed and height of shock formation

The speed of type II radio bursts is determined here through the application of the “hybrid” density model, which was introduced by Vršnak et al. (2004). In their study, the authors evaluated the performance of pre-existing electron density models, specifically the two-fold Saito model (Saito et al., 1970) and the Leblanc model (Leblanc et al., 1998), in terms of their ability to represent the full range of type II radio bursts from the coronal to IP regions. Their findings indicate that neither of these conventional models, whether used individually or in combination, were adequate for accurately characterizing the density in both coronal and IP domain.

To address this limitation and provide a more consistent and

realistic representation of the electron density throughout the entire region of interest, Vršnak et al. (2004) developed the hybrid model. This model was constructed to offer a smooth and continuous transition in the density profile, starting from the low-corona regions associated with active regions and extending outward into the IP medium. One of the key features of the hybrid model is its compatibility with the magnetic field scaling relationship, $B \propto R^{-2}$ (where R is the radial distance), which becomes particularly valid at heliocentric distances beyond $R \approx 2R_s$. This feature ensures that the model remains consistent with observed solar wind magnetic field behavior in the outer corona and IP space. The density model better reflects the physical conditions encountered by type II radio bursts as they propagate through different regions of the solar atmosphere. The final formulation of this newly constructed hybrid model is given by (Vršnak et al., 2004):

$$n[10^8 \text{ cm}^{-3}] = \frac{15.45}{R^{16}} + \frac{3.16}{R^6} + \frac{1}{R^4} + \frac{0.0033}{R^2} \quad (2)$$

After computing the R using density (n) from equations 1 and 2, we found the speed of the type II radio bursts as

$$v = \frac{dR}{dt} = \frac{R_{i+1} - R_i}{t_{i+1} - t_i} \quad (3)$$

where t is the time.

Figure 7 presents the distribution of shock speed and the shock formation height. The figure is divided into two panels for clarity and comparative analysis. The left panel illustrates

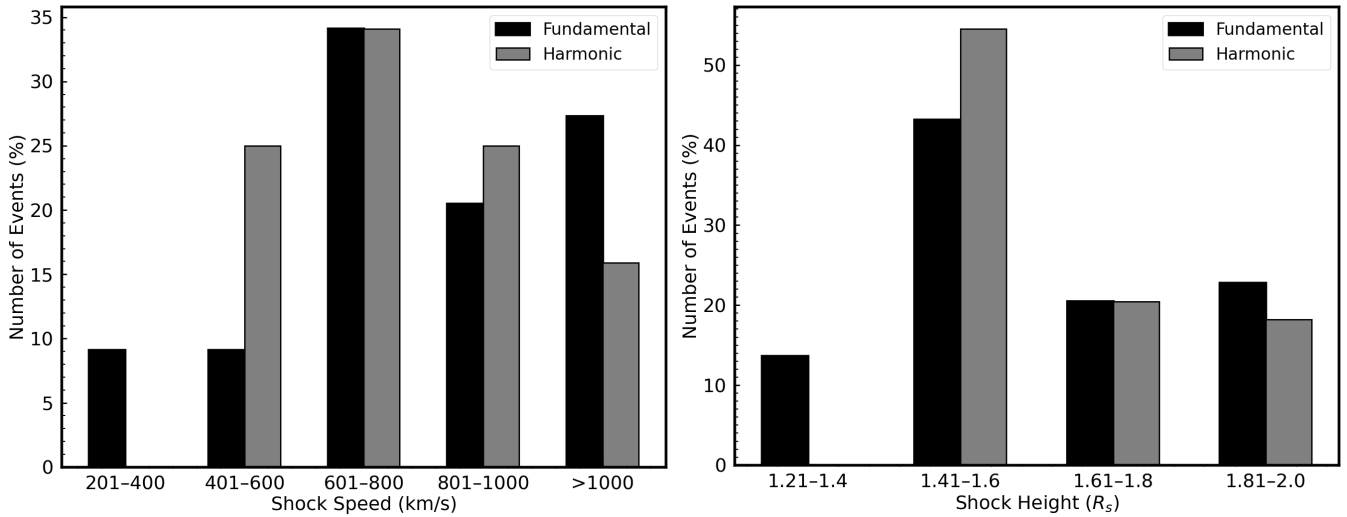


Fig. 7. Distribution of the speed (left) and height (right) of m-type II radio bursts computed from the hybrid model. The speed and height using fundamental and harmonic bands are depicted with black and gray bars, respectively.

the distribution of shock speeds derived from the observed m-type II radio bursts, while the right panel shows the corresponding distribution of shock heights at the onset of these bursts.

The shock speeds (left panel) have been estimated separately for m-type II bursts identified in both the fundamental (black bars) and harmonic (gray bars) bands. The calculated shock speeds span a wide range, from approximately 359 km s^{-1} to 1687 km s^{-1} for the fundamental, and from about 408 km s^{-1} to 1727 km s^{-1} for the harmonic counterparts. It is noticed that nearly one third of the events, i.e., $\approx 34\%$ in both fundamental and harmonic categories fall within the $601 - 800 \text{ km s}^{-1}$ range, indicating that this is the most frequently occurring shock speed range among the analyzed m-type II bursts.

The heights of shock formation (right panel of Figure 7) are determined from the frequency at the LFB of the type II burst at the time of start of type II burst. For the fundamental frequency band, the calculated shock heights range from 1.21 R_s to 2.0 R_s , while for the harmonic band, the corresponding range is slightly narrower, extending from 1.41 R_s to 2.0 R_s . The analysis shows that the majority of the events are concentrated in the $1.41 - 1.6 \text{ R}_s$ range. Specifically, $\approx 43\%$ of the fundamental and an even higher fraction, 55% , of the harmonic band events occur within this height interval. This suggests that a significant number of type II bursts are generated at relatively low coronal heights,

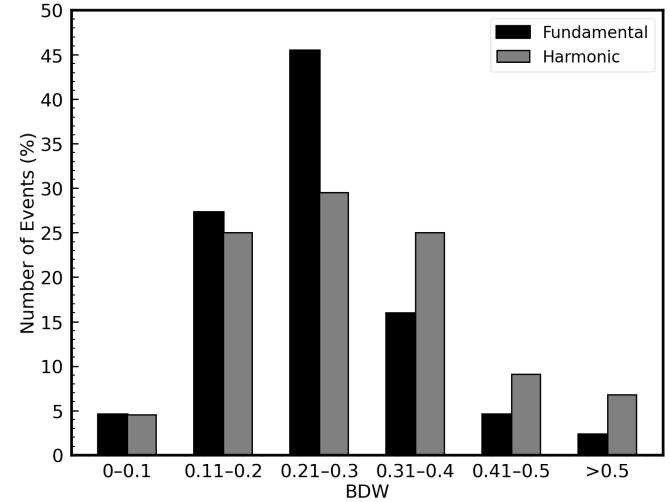


Fig. 8. Distribution of BDW computed from the fundamental (black bars) and harmonic (gray bars) bands.

just above the solar surface, particularly around 1.5 R_s .

3.3.3. Relative band-splitting (BDW)

In our current study, we are using the m-type II radio bursts in which the fundamental and harmonic bands shows splitting. The parameters of this splitting, such as the frequencies and times of the UFBs and LFBs, are used to calculate other coronal parameters. Their values are summarized in Table A.2. The expressions used and the computed parameters are given below.

First, we calculate the relative band-splitting (BDW) which

is given by,

$$BDW = \frac{\Delta f}{f} = \frac{(f_U - f_L)}{f_L} \quad (4)$$

The distribution of relative BDW is presented in Figure 8 with black and gray bars for the fundamental and harmonic bands, respectively. In case of BDW computed from fundamental bands, we obtain the following distribution of events in the respective BDW bins:

- $\approx 45\%$ in $0.21 - 0.3$
- $\approx 27\%$ in $0.11 - 0.2$
- $\approx 16\%$ in $0.31 - 0.4$
- $\approx 12\%$ in $0 - 0.1$ and 0.41 to > 0.5

Similarly, the majority of the BDW values computed from harmonic bands lie in $0.11 - 0.4$, with the following detailed distribution:

- $\approx 25\%$ in $0.11 - 0.2$
- $\approx 30\%$ in $0.21 - 0.3$
- $\approx 25\%$ in $0.31 - 0.4$
- $\approx 20\%$ in 0.41 to > 0.5

The average value of BDW are 0.25 and 0.29, respectively, for fundamental and harmonic bands.

Figure 9 displays the scattered plots of BDW with LFB frequency, i.e., f_L and height of solar corona in panels (a) and (b), respectively. The black and gray colors are chosen for the BDW values from the fundamental and harmonic bands, respectively. To check the relationship of BDW with f_L and the height of the solar corona, we compute the correlation of BDW with these quantities. We find that BDW is very weakly correlated with f_L with a correlation coefficient of -0.25 and -0.39 for the fundamental and harmonic bands, respectively. We also fit a power law in the scattered plots which are written on the top right of the figure. From power law fitting, we find that the $BDW \propto f_L^{-0.430080}$ for fundamental and $BDW \propto f_L^{-0.464667}$ for harmonic band. On the other hand, BDW is weakly correlated to

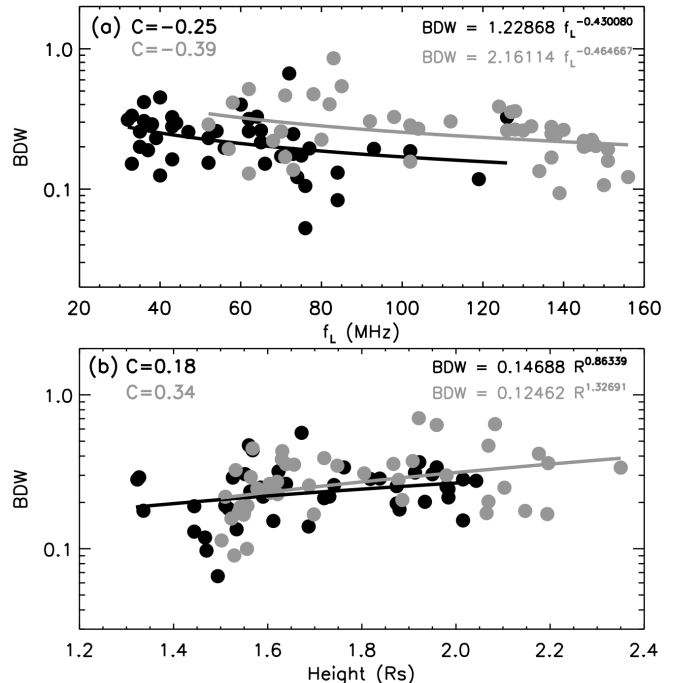


Fig. 9. Scattered plots of BDW versus LFB frequency (top) and radial height of solar corona (bottom). The black and gray dots denotes the BDW values computed from fundamental and harmonic bands, respectively. The black and gray solid lines represents the power law fitting in the data points from fundamental and harmonic bands, respectively. The values of 'C' at the top left of each panel is the Pearson correlation coefficients and at top right is the fitted power law.

the height of the solar corona but with a positive correlation coefficient of 0.18 and 0.34 for fundamental and harmonic bands, respectively. The power law fitting in panel (b) of the figure gives $BDW \propto R^{0.86339}$ for the fundamental and $BDW \propto R^{1.32691}$ for the harmonic band. The low correlation coefficient suggests that the BDW is almost constant over all frequency spectrum and with the height of the solar corona.

3.3.4. Drift rate

The drift rate, denoted as D_f , quantifies the rate of change of frequency over time and is given as:

$$D_f = \frac{f_{start} - f_{end}}{t_{start} - t_{end}}$$

where f_{start} (f_{end}) and t_{start} (t_{end}) are the frequency and time at the start (end) of type II radio burst spectrum, respectively. This calculation is carried out separately for the fundamental and harmonic frequency bands, following a methodology similar to that used in the BDW analysis. After computing the values of D_f for both bands, these values are plotted against the corresponding values of f_L , in order to examine the dependence

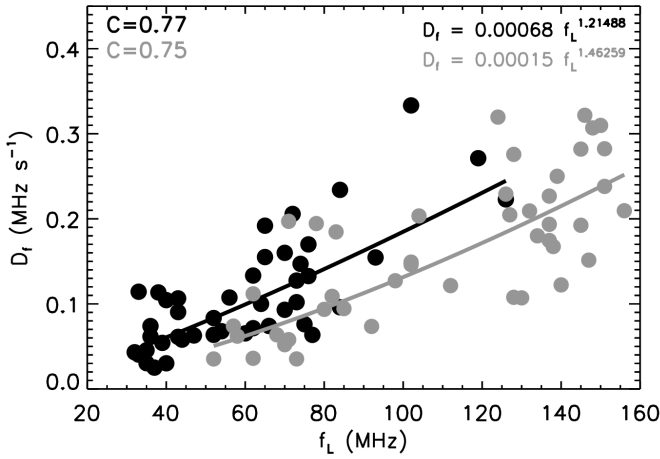


Fig. 10. Variation on drift rate (D_f) with the LFB frequency, f_L shown with black and gray dots. The solid lines are the power law fit to the data. The black and gray colors represents the same as Figure 9. The 'C' at the top right represent the Pearson correlation coefficients for fundamental and harmonic bands with black and gray colors, respectively..

of the drift rate on the LFB frequency. The resulting scatter plot is presented in Figure 10. For consistency, the color notation in this figure is identical to that used in Figure 9. From the plot, we see that D_f increases with an increase in f_L . This trend holds for both the fundamental and harmonic frequency bands, suggesting a positive correlation between these two quantities. To further quantify this relationship, we calculated the linear (Pearson) correlation coefficients which are found to be 0.77 for the fundamental band and 0.75 for the harmonic band, indicating a strong and statistically significant correlation in both cases.

To characterize the nature of this dependency more precisely, we apply a power-law fit to the scatter plot data. The fitted relations give the dependence of D_f on f_L as $D_f \propto f_L^{1.21488}$ and $D_f \propto f_L^{1.46259}$ in case of fundamental and harmonic bands, respectively. These fitted equations, which provide a mathematical description of how the drift rate varies with frequency, are displayed in the upper right corner of Figure 10.

3.3.5. Alfvén Mach number

The Alfvén Mach number (M_A) is computed using the expression (called Rankine-Hugoniot jump relation) suggested by Vršnak et al. (2002), which is given as follows:

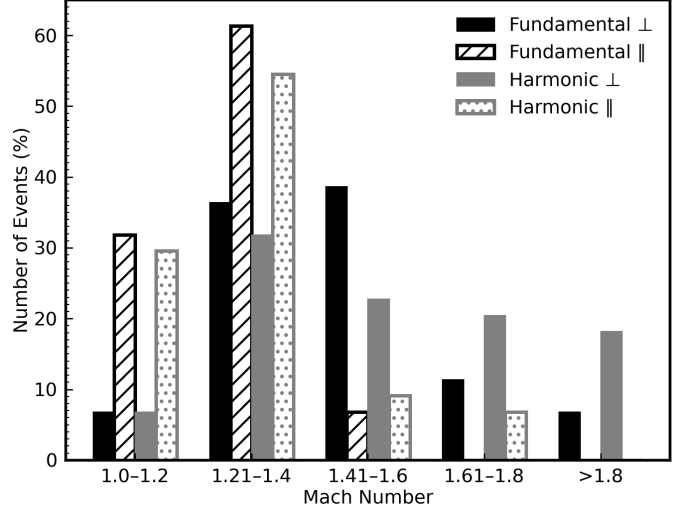


Fig. 11. Histogram of mach number computed separately for fundamental and harmonic bands of m-type II radio bursts.

$$M_A = \begin{cases} \sqrt{\frac{X(X+5)}{2(4-X)}}, & \text{for perpendicular shock} \\ \sqrt{X}, & \text{for parallel shock} \end{cases} \quad (5)$$

Here, X is the density jump that can be calculated using the band splitting in type II bands. It is given by the relation $X = \left(\frac{f_U}{f_L}\right)^2$. Now, as frequency and density are related to each other through the relation $f \propto \sqrt{n}$, presented in Equation 1, using the latter and Equation 4, the density jump (X) can be expressed as

$$X = \left(\frac{f_U}{f_L}\right)^2 = \frac{n_2}{n_1} = (BDW + 1)^2 \quad (6)$$

Using the above equations, we computed the density jump (X) and the Alfvén Mach number (M_A). This gives different values for fundamental and harmonic bands as the frequencies are different in these bands. No information is available whether the shock driver of the type II radio bursts is perpendicular or parallel. Therefore, for completeness, we computed the M_A using both formulae. In this way, we obtain two values of M_A for fundamental and two for harmonic bands, viz., one for perpendicular and one for parallel shock, i.e., in total four values of M_A for a single event. The histogram of the computed M_A with the number of events is presented in Figure 11. The four different values are plotted in different color-coded bars, as explained in the figure legend, namely, the black solid bar and the bar with black slant lines represent the M_A

derived from the fundamental band considering perpendicular and parallel shocks, respectively. Similarly, solid gray bar and the bar with gray dots represent the M_A derived from the harmonic band considering the perpendicular and parallel shocks, respectively.

Below we explain the distribution of fundamental and harmonic bands with perpendicular and parallel shocks. In the case of M_A calculated from the fundamental band with perpendicular shock (black solid bars), the majority of the events ($\approx 82\%$) lie in the range $1 - 1.6$. The remaining events are in the range $1.61 - 2.5$, with the maximum value of $M_A \approx 2.5$. For parallel shocks (bars with black slant lines), $\approx 93\%$ of the events have M_A in the range $1 - 1.4$. The maximum value of M_A in this case is ≈ 1.57 .

On the other hand, the M_A computed from the harmonic band with perpendicular shock (gray solid bars) is distributed as follows: $\approx 32\%$ for this case lie in the range $1.21 - 1.4$ and almost an equal number of events are distributed in the range $1.41 - 1.6$ ($\approx 20\%$) and $1.61 - 1.8$ ($\approx 22\%$). A similar distribution is shown by the M_A calculated from parallel shock (gray bars with dots), in the sense that most of events ($\approx 55\%$) lie in the range of $1.21 - 1.4$. However, the number of events for the smallest values of M_A , $1.0 - 1.2$, is significantly higher, about 30% , which is ≈ 1.7 times more compared to the case of perpendicular shock. The maximum value of M_A in this case is 1.7 .

3.3.6. Alfvén speed

After the computation of M_A , its values are used to calculate the Alfvén speed using the following equation:

$$v_A = \frac{v}{M_A} \quad (7)$$

where v is the speed of the type II radio bursts, i.e., shock speed. We calculated the Alfvén speed separately for the fundamental and harmonic bands, considering both types of shocks, viz., perpendicular and parallel, shown in Figure 12. The color-code used, namely, solid black and gray bars, black bars with slant lines, gray bars with dots, is similar to that in Figure 11.

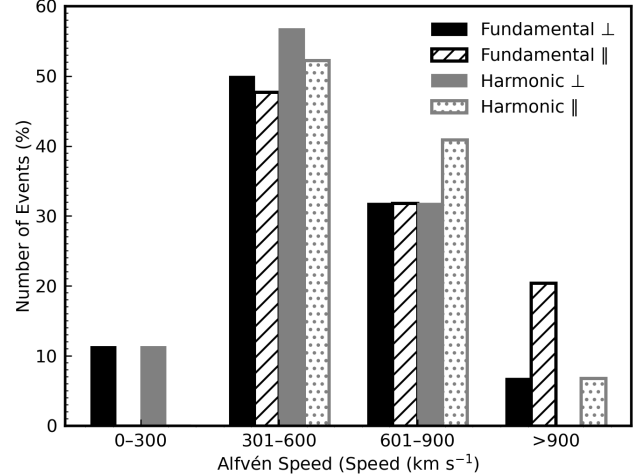


Fig. 12. Histograms of Alfvén speed computed from fundamental and harmonic bands of m-type II radio bursts.

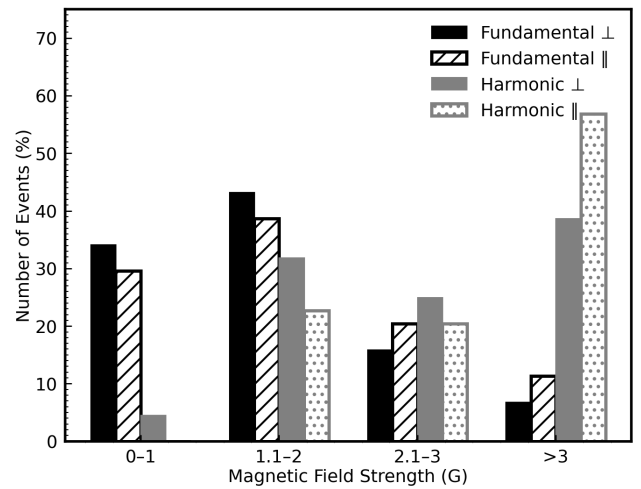


Fig. 13. Distribution of magnetic field strength calculated for perpendicular and parallel shock using fundamental and harmonic bands in type II bursts.

From the figure, we see that the majority of events in each case, i.e., $> 48\%$, have the Alfvén speed in the range $301 - 600$ km s^{-1} . The bin of $601 - 900$ km s^{-1} have more than $\approx 32\%$ of events in this range. As far as the minimum and maximum values of Alfvén speed is concerned, it ranges from $267 - 1071$ km s^{-1} for fundamental bands with perpendicular shock, $301 - 1294$ km s^{-1} for fundamental bands with parallel shock, $233 - 861$ km s^{-1} for harmonic bands with perpendicular shock, and $316 - 1177$ km s^{-1} for harmonic bands with parallel shock.

3.3.7. Coronal magnetic field

Insofar, the values of all the coronal parameters calculated in the above subsections are present. These parameters are used to

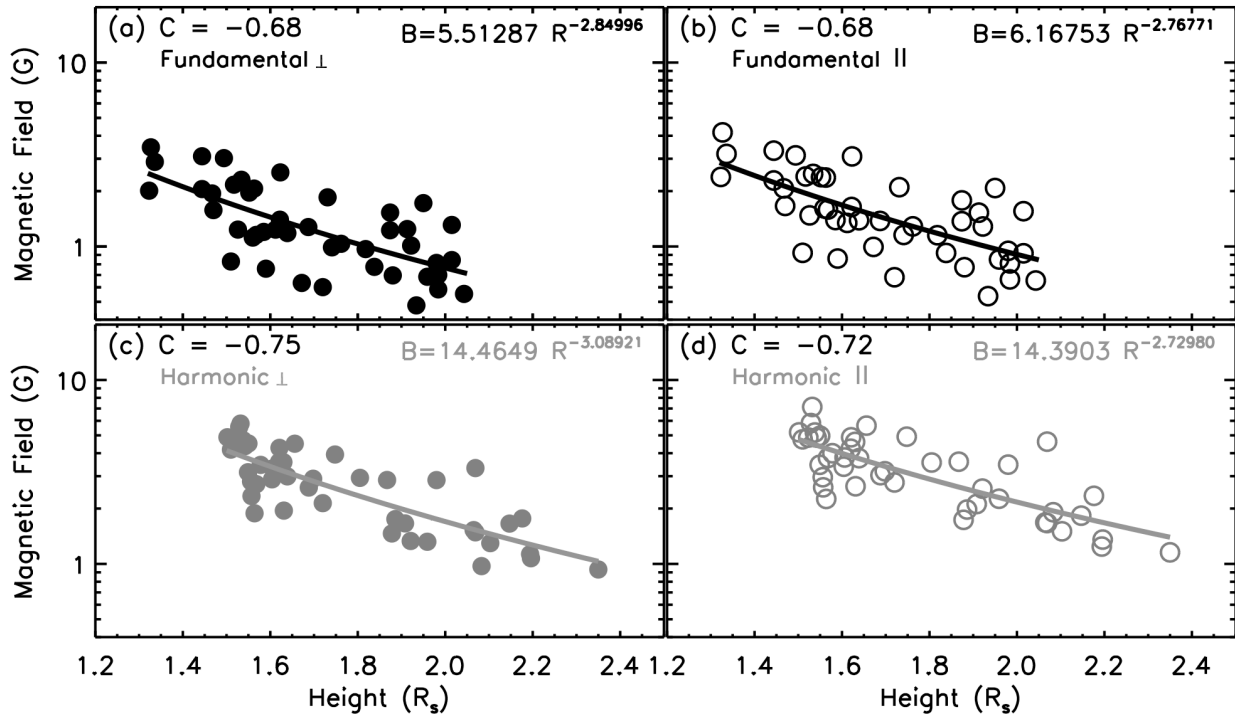


Fig. 14. Variation of coronal magnetic field strength with radial distance from the Sun computed from fundamental and harmonic bands in top and bottom panels, respectively. The filled and empty circles represent the magnetic field strength from the perpendicular and parallel shocks, respectively. The power law fit are shown with solid lines in each panel.

find the coronal magnetic field strength using the following expression (Vršnak et al., 2002; Gopalswamy et al., 2012b; Vasanth et al., 2014),

$$B = 5.1 \times 10^{-5} \times f \times v_A \quad (8)$$

where the magnetic field B is in Gauss (G), f and v_A in MHz and km s^{-1} , respectively. The frequency is taken as the average of the frequencies at the beginning and end of the type II burst, that is, $f = (f_{\text{start}} + f_{\text{end}})/2$. As we have the values of v_A from the fundamental band perpendicular and parallel shocks, and the harmonic band perpendicular and parallel shocks, we get four values of B for a single event.

The distribution of the computed values of B using equation 8 are plotted in Figure 13. The colors of the bars in left panel have the same meaning as in Figures 11 and 12. The B computed from the fundamental bands is lower than that from the harmonic bands. From the figure, it is seen that the majority of events (> 40 %) have B in range of 1.1 – 2 G, both in case of perpendicular and parallel shock. However, in the case of harmonic bands, B is > 3 G for the majority events (> 39 %).

We also plotted the variation of B with the radial distance of the Sun in Figure 14. The filled dots (panel (a)) and empty circles (panel (b)) denote the B computed from the fundamental band with perpendicular and parallel shock, and gray dots (panel (c)) and gray empty circles (panel (d)) from the harmonic with perpendicular and parallel shock, respectively. This figure again confirms that the value of B from fundamental bands is less than that from the harmonic bands.

Overall, B decreases with the height of solar corona, i.e., with an increase in radial distance from the Sun, regardless of fundamental or harmonic band, and perpendicular or parallel shock. In order to quantify the correlation between the computed magnetic field and the radial distance, we used the linear (Pearson) correlations. We found a negative correlation coefficient of $\approx -0.68, -0.68, -0.75$, and -0.72 in case of magnetic field calculated from fundamental using a perpendicular shock, fundamental using parallel shock, harmonic using a perpendicular shock, and harmonic using parallel shock, respectively. In summary, the magnetic field is inversely correlated to the radial

distance of the Sun. Finally, the power law fitting to these data led to $B \propto R^{-2.85}$, $B \propto R^{-2.77}$, $B \propto R^{-3.09}$, and $B \propto R^{-2.73}$, respectively.

4. Discussion

4.1. CMEs and flares as type II burst drivers

It is believed that when a CME moves fast enough, it can drive a shock wave ahead of it. This occurs when the CME surpasses the local Alfvén speed – the characteristic speed at which magnetic disturbances travel through the solar plasma. Previous studies have reported a robust association between DH-type II bursts and CMEs at 1 AU (Sheeley et al., 1985). However, in the lower corona, the connection between m-type II bursts and CMEs appears less consistent (Sheeley et al., 1985; Gopalswamy et al., 1998; Reiner et al., 1999; Gopalswamy et al., 2008). Our present analysis specifically investigates m-type II radio bursts that exhibit a band-splitting in both the fundamental and harmonic components. Band-splitting is often considered a signature of strong shocks. Our results indicate that 41 out of 44 m-type II events ($\approx 93\%$) are associated with CMEs. This high association rate implies that strong m-type II bursts – particularly those with band-splitting – are closely linked to CME-driven shocks.

Furthermore, Michalek et al. (2007) proposed that fast and wide CMEs are more likely to be associated with type II radio bursts compared to their slower, narrower counterparts. Our findings support this interpretation. The substantial majority of the CMEs in our sample are wide CMEs, among them 12 are halo and 10 are partial-halo (i.e., angular width $> 120^\circ$ but $< 360^\circ$, as defined in Gopalswamy et al., 2010) CMEs, as illustrated in Figure 5(c). These halo events exhibit high velocities, ranging from 555 to 2625 km s^{-1} , whereas non-halo CMEs tend to fall within a slower speed range of 215 to 830 km s^{-1} . This supports the conclusion that fast, wide (halo) CMEs are more effective at generating strong shocks capable of producing type II radio emissions.

All of m-type II cases in our study were also associated with solar flares, thus a flare-contribution cannot be excluded in ei-

ther case. As far as the location of type II sources on the solar disk is concerned, it is found that majority of events are originated from the southern hemisphere (see Figure 4), which confirms the north-south asymmetry (Carbonell et al., 1993). This is due to the southern dominance of solar activity in solar cycle 24, as reported in previous studies using different data sets, namely, flares, CMEs, Sunspots, solar energetic particles, etc. (Chandra et al., 2013; Li et al., 2019; Samwel & Miteva, 2021; Zhang et al., 2023).

4.2. Non-CME drivers of type II bursts

To explain the remaining two m-type II radio bursts without CMEs, there can be other possibilities drives. These possibilities include EUV waves, and small scale jet events (Magdalenić et al., 2008; Pohjolainen et al., 2008; Magdalenić et al., 2012; Maguire et al., 2021; Morosan et al., 2023). In our case, we have found three events (event no. 12, 20, and 28 in Table A.1) that are not associated with CMEs. In event no. 12, the type II radio burst could be produced by the associated flare only, i.e. the type II bursts is clearly due to a flare pressure pulse, since a CME could not be isolated. Morosan et al. (2023) did a detailed study of event no. 20 and found that this type II radio burst is generated by coronal wave, that steepens into a shock wave, associated with the C-class flare. The event no. 28 was associated with a very weak flare of B-class. Therefore, there is a high chance that this type II bursts is not produced by the associated flare. On careful examination of the event, we find that a jet is associated with this flare. Therefore, this jet activity can be a possible generation of the type II shock.

4.3. Type II band splitting and BDW

For the computation of BDW, Tsap et al. (2020) took the pixel coordinates and then converted them into digital values. In our case, the estimation of the type II properties is done by eye and is based on the visible length of the type II bands, namely by taking values at the start and end of the spectra. In such a way, the results are an approximation and could be considered

as averaged values, representative for the entire duration of the bursts.

The values of BDW in our study range from 0.06 – 0.57 and 0.09 – 0.70 in the case of fundamental and harmonic bands, respectively. The average value of BDW for fundamental bands is 0.25 and for harmonic band it is 0.29. In Mann et al. (1996), the average value of BDW is 0.32 in m-domain. Moreover, in DH-km domain studied by Aguilar-Rodriguez et al. (2005) the value of BDW for type II radio bursts from different instruments varies from 0.26 – 0.5. Our values of BDW are slightly different from that of Mann et al. (1996) but are well in range of Aguilar-Rodriguez et al. (2005). Also, from Figure 9, we see that the BDW does not change much with the frequency (or wavelength) and radial distance. This is because the change in frequency depends on the change in density as $\Delta f/f = \Delta n/2n$ (Lengyel-Frey & Stone, 1989), and the density fluctuation structure is almost the same for the entire spectral domain (Vršnak et al., 2001, 2002; Aguilar-Rodriguez et al., 2005).

The power law fitting in the scattered plots of BDW with frequency (f_L) and radial distance (R) suggest that the BDW varies as $BDW \propto f_L^{\sim -0.4}$ and $BDW \propto R^{\sim 1}$. This is consistent to the results obtained in previous studies (for example, Vršnak et al., 2001, 2004; Aguilar-Rodriguez et al., 2005).

4.4. Drift rate

The frequency drift rate (D_f) of type II radio bursts characterizes how the emission frequency changes with time, reflecting the motion of the shock through the solar corona or IP medium. In the present study, the computed values of D_f cover approximately from 0.03 to 3.4 MHz s⁻¹. This range fall well within the range reported by Vršnak et al. (2002), affirming the reliability of our analysis. Furthermore, we find a strong power-law relationship between D_f and the corresponding frequency f_L , expressed as $D_f \propto f_L^{\sim 1.5}$. The strength of this correlation is supported by a correlation coefficient (C) of ≥ 0.75 . These findings are broadly consistent with those of Vršnak et al. (2002), who reported a similar power-law dependence of $D_f \propto f_L^{1.89}$

and a higher correlation coefficient ($C = 0.93$), indicating a robust link between D_f and the local plasma frequency, f_L . This consistency reinforces the interpretation that higher frequencies, which correspond to denser coronal regions, are associated with more rapid D_f due to steeper plasma density gradients.

In contrast, Mann et al. (1995) reported significantly lower values of D_f , in the range of 0.04 – 0.46 MHz s⁻¹, likely due to the selection of events associated with weaker shocks. This discrepancy highlights the variability in D_f depending on the coronal conditions (see also Reiner et al., 1999; Magdalenić et al., 2012).

4.5. Alfvén Mach number

The Alfvén Mach number (M_A) is a key parameter to describe the strength of a shock. It is reported that the large values of M_A can easily generate type II radio bursts (Shen et al., 2007; Su et al., 2016). However, Mann et al. (2022) found the M_A to be in the range 1.59 – 2.53. They concluded that this moderate M_A is capable of accelerating electrons to energies high enough to excite Langmuir waves, and hence the type II radio bursts. The computed values of the M_A in our study for fundamental and harmonic bands considering perpendicular and parallel shocks are in range 1.10 – 3.38. These values of M_A are consistent with those computed in previous studies (Vršnak et al., 2002; Warmuth & Mann, 2005; Su et al., 2016; Magdalenić et al., 2020; Mann et al., 2022). In addition to statistical studies, the obtained here M_A range is corroborated by case studies (Zucca et al., 2014; Su et al., 2016). The computed values of M_A are always high in case of parallel shock. This could be due to the Buneman instability (as described in the model of Chernov & Fomichev, 2021), according to which the shock wave can only be strictly perpendicular. If it deviates from the perpendicular by an angle of $> 2^\circ$, the radiation stops. At the same time, the radiation from the parallel front is much weaker (Zaitsev, 1977). Additionally, for the fundamental bands, there are only two events for which the M_A is greater than 2 (i.e., 2.15 and 2.47), whereas in the case of harmonic bands, the events are three (with values 2.80, 3.29, and 3.37). These deviations from the theoretical results for perpendicular shock (namely values

below 2, e.g., Priest, 1982), could be due to the inconsistencies in the adopted visual procedure while selecting the frequency and time of the splitted bands.

4.6. Alfvén speed and coronal magnetic field

Previous studies have reported a range of Alfvén speeds and magnetic field strengths computed using the type II radio bursts and other phenomena. For instance, Vršnak et al. (2002) analyzed 18 metric type II events with band splitting and found Alfvén speeds ranging from 400 to 500 km s⁻¹ at a heliocentric distance of $\approx 2 R_s$, increasing to 450 – 700 km s⁻¹ at $\approx 2.5 R_s$. Cho et al. (2007) studied the 18 August 2004 event and computed the Alfvén speed and magnetic field strength using type II radio burst from Green Bank Solar Radio Burst Spectrometer (GBSRBS), associated CME from Mauna Loa Solar Observatory and, using Potential Field Source Surface (PFSS) extrapolation. They reported Alfvén speeds in the range of 400 – 550 km s⁻¹ and magnetic field strengths between 0.4 and 1.3 G, varying from a height of 1.4 to 2.1 R_s. A case study conducted by Gopalswamy et al. (2012b), combining type II burst data and extreme-ultraviolet images, found a lower value of Alfvén speeds (i.e., 140 – 460 km s⁻¹) and magnetic fields between 1.3 and 1.5 G at heights of 1.2 – 1.5 R_s. Similarly, Vasanth et al. (2014) reported magnetic fields of 2.7 – 1.7 G over 1.3 – 1.5 R_s, and Alfvén speeds of 406 – 600 km s⁻¹.

In comparison, the values obtained in our study show a broad range of Alfvén speeds and magnetic field strengths, considering both perpendicular and parallel shocks. The Alfvén speeds in our analysis is in the range 268 – 1294 km s⁻¹ and 233 – 1177 km s⁻¹ for fundamental and harmonic bands, respectively. The magnetic field strengths span from 0.48 – 4.17 G for fundamental, and 0.9 – 7.13 G for harmonic band.

Overall, while our Alfvén speed and magnetic field estimates are consistent with the physical expectations from type II burst-related shock scenarios, they tend to be higher than those from earlier studies. The possible reasons could be different local coronal conditions, measurement techniques, or variations in heliocentric distance and plasma environment. The power law fitting in the variation of magnetic field strength with the radial

distances gives an estimate of the magnetic field dependence on the radial distance. This is done by Vršnak et al. (2002) and Vršnak et al. (2004). It is found that the power law fit as $B \propto R^{-3.4}$ in case of former, whereas, it varies as $B \propto R^{-1.75}$ to $B \propto R^{-2.23}$ in the latter. The power-law fit of our current study fits well in this range considering both perpendicular and parallel shocks for the splitting in fundamental and harmonic bands. These values lies in the range $B \propto R^{-2.78}$ – $B \propto R^{-2.85}$ and $B \propto R^{-2.73}$ – $B \propto R^{-3.09}$ for fundamental and harmonic bands, respectively.

The observed discrepancies in the deduced plasma parameters from the fundamental and harmonic bands could be due to a multitude of effects, a combination of several underlying emission mechanisms or/and limitations of the applied methodology and theory.

5. Summary

Based on the 44 m-type II bursts exhibiting band-splitting analyzed in solar cycle 24 (2009 – 2019), the following trends were identified in this study:

- Six out of 44 (13%) band-splitting bursts are associated with X-class flares and only three of them continued as DH-type II.
- Shock speeds deduced for the fundamental band show a preference towards lower values (with the majority of cases within the range 401 – 1000 km s⁻¹), compared to the harmonic emissions that tends to give higher shock speeds (from 601 to >1000 km s⁻¹).
- The same results for the shock heights are obtained, independent on fundamental or harmonic emission data used: a significant number of the shock waves are forming at low coronal heights (1.41 – 1.6 R_S).
- BDW is nearly constant over the entire frequency spectrum and with the height of solar corona.
- Alfvén Mach number at predominantly lower values (below 1.4) are obtained for parallel shocks, whereas for the

perpendicular shocks, the Mach number distribution starts with a peak (over the range 1.21 – 1.6) ending with a slow decline (independent on the fundamental or harmonic bands in either case).

- Alfvén speed values tend to cover almost entirely the range $\approx 230 - 1230$ km s $^{-1}$ in either combination of the fundamental/harmonic band with a parallel/perpendicular shock wave.
- Magnetic field strength for the fundamental band tends to be at lower values, in most cases below 2 G, whereas for the harmonic band it is above 2 G, independent of the shock type.

All these results are obtained for the first time on a large time scale i.e., for the entire solar cycle 24. Some of these results confirm the previously known ones. They are a reliable aid for further theoretical research.

Appendix A. Details of All Events

In the appendix, we present a table of the list of events chosen for current our study. All the events have splitting in both fundamental and harmonic bands of the dynamic radio spectra. The table also includes details about the associated flares (such as their GOES class, onset, peak, and end times), CMEs (onset, speed, acceleration, and angular width), and the DH-type II radio bursts (see Table A.1). The measured frequencies at different times from the fundamental and harmonic bands are presented in Table A.2.

Acknowledgments

The authors thank Dr. G. P. Chernov and the other anonymous reviewer for their valuable comments and suggestions on the manuscript. We thank the open data policy of RSTN, GOES, and SOHO for their open data policy. RC acknowledges the support from the DST/SERB project number EEQ/2023/000214. PD acknowledges the support by the Research Council of Norway through its Centres of Excellence scheme, project number 262622.

References

Aguilar-Rodriguez, E., Gopalswamy, N., MacDowall, R. et al. (2005). A universal characteristic of type II radio bursts. *Journal of Geophysical Research (Space Physics)*, 110(A12), A12S08. doi:10.1029/2005JA011171.

Carbonell, M., Oliver, R., & Ballester, J. L. (1993). On the asymmetry of solar activity. *Astron. Astrophys.*, 274, 497.

Chandra, R., Gopalswamy, N., Mäkelä, P. et al. (2013). Solar energetic particle events during the rise phases of solar cycles 23 and 24. *Advances in Space Research*, 52(12), 2102–2111. doi:10.1016/j.asr.2013.09.006.

Chernov, G., & Fomichev, V. (2021). On the Issue of the Origin of Type II Solar Radio Bursts. *Astrophys. J.*, 922(1), 82. doi:10.3847/1538-4357/ac1f32.

Cho, K. S., Lee, J., Gary, D. E. et al. (2007). Magnetic Field Strength in the Solar Corona from Type II Band Splitting. *Astrophys. J.*, 665(1), 799–804. doi:10.1086/519160.

Chrysaphi, N., Kontar, E. P., Holman, G. D. et al. (2018). CME-driven Shock and Type II Solar Radio Burst Band Splitting. *Astrophys. J.*, 868(2), 79. doi:10.3847/1538-4357/aae9e5.

de Groot, T. (1960). Dynamic spectra and polarization of small bursts in solar radio emission. *Bull. Astron. Inst. Netherlands*, 15, 229.

Devi, P., Miteva, R., Chandra, R. et al. (2024). Type II radio bursts and space weather phenomena: A statistical study. *Advances in Space Research*, 74(10), 5263–5281. doi:10.1016/j.asr.2024.07.072.

Fomichev, V. V. (1972). Propagation through the Solar Corona of the Shock Waves Responsible for Type II Radio Bursts. *Soviet Astron.*, 16, 284.

Frassati, F., Susino, R., Mancuso, S. et al. (2019). Comprehensive Analysis of the Formation of a Shock Wave Associated with a Coronal Mass Ejection. *Astrophys. J.*, 871(2), 212. doi:10.3847/1538-4357/aae9af.

Ginzburg, V. L., & Zhelezniakov, V. V. (1958). On the Possible Mechanisms of Sporadic Solar Radio Emission (Radiation in an Isotropic Plasma). *Soviet Astron.*, 2, 653.

Gopalswamy, N., Hanaoka, Y., Kosugi, T. et al. (1998). On the relationship between coronal mass ejections and magnetic clouds. *Geophys. Res. Lett.*, 25(14), 2485–2488. doi:10.1029/98GL50757.

Gopalswamy, N., Mäkelä, P., Akiyama, S. et al. (2012a). Radio-loud CMEs from the disk center lacking shocks at 1 AU. *Journal of Geophysical Research (Space Physics)*, 117(A8), A08106. doi:10.1029/2012JA017610.

Gopalswamy, N., Mäkelä, P., & Yashiro, S. (2019). A Catalog of Type II radio bursts observed by Wind/WAVES and their Statistical Properties. *Sun and Geosphere*, 14, 111–121. doi:10.31401/SunGeo.2019.02.03.

Gopalswamy, N., Nitta, N., Akiyama, S. et al. (2012b). Coronal Magnetic Field Measurement from EUV Images Made by the Solar Dynamics Observatory. *Astrophys. J.*, 744(1), 72. doi:10.1088/0004-637X/744/1/72.

Gopalswamy, N., Yashiro, S., Michalek, G. et al. (2009). The SOHO/LASCO CME Catalog. *Earth Moon and Planets*, 104(1-4), 295–313. doi:10.1007/s11038-008-9282-7.

Gopalswamy, N., Yashiro, S., Michalek, G. et al. (2010). A Catalog of Halo Coronal Mass Ejections from SOHO. *Sun and Geosphere*, 5(1), 7–16.

Gopalswamy, N., Yashiro, S., Xie, H. et al. (2008). Radio-Quiet Fast and Wide Coronal Mass Ejections. *Astrophys. J.*, 674(1), 560–569. doi:10.1086/524765.

Holman, G. D., & Pesses, M. E. (1983). Solar type II radio emission and the shock drift acceleration of electrons. *Astrophys. J.*, 267, 837–843. doi:10.1086/160918.

Lawrance, B., Devi, P., Chandra, R. et al. (2024). A Catalogue of Metric Type II Radio Bursts Detected by RSTN During Solar Cycle 24. *Solar Phys.*, 299(75). doi:<https://doi.org/10.1007/s11207-024-02317-8>.

Leblanc, Y., Dulk, G. A., & Bougeret, J.-L. (1998). Tracing the Electron Density from the Corona to 1 au. *Solar Phys.*, 183(1), 165–180. doi:10.1023/A:1005049730506.

Lengyel-Frey, D., & Stone, R. G. (1989). Characteristics of interplanetary type II radio emission and the relationship to shock and plasma properties. *J. Geophys. Res.*, 94(A1), 159–167. doi:10.1029/JA094iA01p00159.

Li, F. Y., Xiang, N. B., Xie, J. L. et al. (2019). The Present Special Solar Cycle 24: Casting a Shadow over Periodicity of the North-South Hemispherical Asymmetry. *Astrophys. J.*, 873(2), 121. doi:10.3847/1538-4357/ab06bf.

Magdalenić, J., Marqué, C., Fallows, R. A. et al. (2020). Fine Structure of a Solar Type II Radio Burst Observed by LOFAR. *Astrophys. J. Lett.*, 897(1), L15. doi:10.3847/2041-8213/ab9abc.

Table A.1. Details of band splitted m-Type II radio bursts. The Table also presents the details of associated flares, CMEs, and DH-type II parameters. ('*' denote the associated CME on next day.)

Event	m-type II Burst			Associated Flare			Associated CME			Associated	
	No.	Date	Onset	Onset	GOES	Location	Onset	Speed	Acceleration	Angular width	DH-type II/
			DD-MM-YYYY	(UT)	(UT)	Class	(UT)	(km s ⁻¹)	(m s ⁻²)	(degree)	Onset (UT)
1	13-06-2010	05:40	05:30	M1.0	S24W91	06:06	320	4.8	16	360	No
2	16-10-2010	19:15	19:07	M2.9	S19W29	20:12	350	47	32	360	No
3	12-11-2010	01:35	01:28	C4.6	S22W11	02:24	245	-0.9	61	360	No
4	25-03-2011	23:15	23:08	M1.0	S16E30	01:25*	339	-6.6	12	360	No
5	18-01-2012	23:20	22:57	C5.1	N24W47	23:48	270	-2	119	360	No
6	26-03-2012	—	—	—	Backside	23:12	1390	-32.3	360	23:15	No
7	24-04-2012	07:45	07:38	C3.7	N14E58	08:12	443	-8.1	192	360	No
8	03-06-2012	18:00	17:48	M3.3	N16E33	18:12	605	-8.7	180	360	No
9	02-07-2012	05:00	05:01	C3.5	S17E03	06:00	251	-1.6	90	360	No
10	06-07-2012	23:10	23:01	X1.1	S17W50	23:24	1828	-56.1	360	23:10	No
11	12-07-2012	16:25	15:37	X1.4	S17W08	16:48	885	195.6	360	16:45	No
12	25-09-2012	04:30	04:24	C3.6	N09E03	No CME	—	—	—	360	No
13	08-11-2012	02:20	02:08	M1.7	N12W71	02:36	855	-15.2	360	360	No
14	12-11-2012	23:30	23:13	M2.0	S21E43	00:54	611	3.9	45	360	No
15	28-04-2013	20:15	19:46	C4.4	S16W44	20:48	497	-23.3	91	360	No
16	02-05-2013	05:05	04:58	M1.1	N09W31	05:24	671	1.1	99	360	No
17	14-05-2013	01:05	01:00	X3.2	N12E67	01:25	2625	-51	360	01:16	No
18	03-07-2013	07:04	07:00	M1.5	S14E56	07:24	807	-26.1	267	360	No
19	25-10-2013	03:00	02:48	M2.9	S08E59	03:24	344	-3.9	121	360	No
20	25-10-2013	13:35	13:29	C2.3	N08W37	No CME	—	—	—	360	No
21	08-11-2013	04:25	04:20	X1.1	S11W03	05:12	409	-5.7	105	360	No
22	08-01-2014	03:40	03:39	M3.6	N11W91	04:12	643	-3.7	108	360	No
23	11-02-2014	03:30	03:22	M1.7	S13W00	04:12	222	1.4	81	360	No
24	20-02-2014	03:20	02:48	C3.3	S11E32	03:12	993	-48.8	360	08:05	No
25	20-02-2014	07:45	07:26	M3.0	S14W81	08:00	948	-9.5	360	08:05	No
26	20-03-2014	04:00	03:42	M1.7	S15E27	04:36	740	-2	360	360	No
27	01-08-2014	18:20	17:55	M1.5	S09E08	18:36	789	-15.2	360	18:58	No
28	22-08-2014	00:05	00:03	B8.0	N05E13	No CME	—	—	—	360	No
29	25-08-2014	15:10	14:46	M2.0	N09W47	15:36	555	-12.2	360	15:20	No
30	07-09-2014	02:00	01:53	C7.5	S20E46	02:24	487	-10.7	104	360	No
31	23-09-2014	23:10	23:03	M2.3	S11E36	23:36	331	18.6	134	360	23:41
32	28-09-2014	02:45	02:39	M5.1	S17W40	03:24	215	5.5	60	360	No
33	02-10-2014	19:00	18:49	M7.3	S14W91	19:12	513	-0.5	159	360	21:34
34	05-11-2014	09:40	09:26	M7.9	N15E53	10:00	386	-3	182	360	No
35	07-11-2014	17:20	16:53	X1.6	N15E33	18:08	795	-24.4	293	360	No
36	17-12-2014	04:40	04:25	M8.7	S19W02	05:00	587	-2.1	360	05:00	No
37	20-12-2014	00:40	00:11	X1.8	S18W42	01:25	830	-8.5	257	360	No
38	09-03-2015	23:40	23:29	M5.8	S17E39	00:00*	995	-10.2	360	360	No
39	21-12-2015	01:00	00:52	M2.8	N04E85	01:26	389	-4.7	71	360	No
40	23-12-2015	00:30	00:23	M4.7	S23E49	01:25	520	1.6	89	360	01:18
41	02-05-2016	08:40	08:32	C3.5	N21E24	09:12	262	-3.7	61	360	No
42	04-05-2016	12:55	13:41	C1.3	N11W91	14:12	390	-3.4	134	360	14:20
43	10-07-2016	01:00	00:53	C8.6	N09E49	01:25	368	-2.5	101	360	No
44	20-10-2017	23:30	23:10	M1.1	S11E91	00:00*	331	-2.8	109	360	No

Table A.2. Band splitting parameters of the fundamental and harmonic bands.

Event	Fundamental Band						Harmonic Band						
	Date	Start			End			Start			End		
		UFB (MHz)	LFB (MHz)	Time (UT)	UFB (MHz)	LFB (MHz)	Time (UT)	UFB (MHz)	LFB (MHz)	Time (UT)	UFB (MHz)	LFB (MHz)	
(DD-MM-YYYY)													
13-06-2010		82	62	05:40:35	46	38	05:45:02	171	137	05:39:36	59	49	05:47:50
16-10-2010		133	119	19:13:32	82	56	19:16:40	178	148	19:14:17	120	83	19:17:26
12-11-2010		91	73	01:40:46	60	45	01:45:50	152	134	01:40:46	98	92	01:45:46
25-03-2011		111	93	23:17:30	45	38	23:24:37	175	151	23:18:44	85	70	23:25:02
18-01-2012		38	33	23:24:50	30	26	23:28:08	68	57	23:26:10	51	44	23:30:00
26-03-2012		88	75	22:50:10	53	30	22:57:50	164	130	22:50:35	96	60	23:01:10
24-04-2012		45	40	07:48:24	39	26	07:51:43	115	78	07:48:40	45	40	07:54:40
03-06-2012		68	54	18:01:09	34	27	18:09:30	131	85	18:00:30	52	30	18:14:26
02-07-2012		95	84	05:09:47	62	55	05:12:08	166	150	05:09:53	87	81	05:14:08
06-07-2012		44	33	23:11:20	32	26	23:13:05	104	71	23:10:26	50	34	23:15:00
12-07-2012		44	37	16:27:48	34	28	16:34:27	82	58	16:27:57	47	36	16:37:21
25-09-2012		80	76	04:29:43	54	50	04:32:16	160	137	04:29:07	106	91	04:33:46
08-11-2012		64	52	02:22:02	39	27	02:28:35	120	92	02:21:50	49	39	02:37:56
12-11-2012		78	62	23:29:30	53	45	23:35:20	159	126	23:29:30	96	80	23:34:05
28-04-2013		51	36	20:19:45	34	27	20:23:35	83	68	20:19:47	45	38	20:29:44
02-05-2013		47	36	05:08:24	30	25	05:13:00	154	83	05:07:15	70	45	05:14:50
14-05-2013		84	60	01:09:35	52	30	01:17:45	180	147	01:08:35	102	61	01:17:10
03-07-2013		58	40	07:13:20	32	25	07:17:29	132	104	07:14:00	84	59	07:17:56
25-10-2013		57	44	03:00:38	37	29	03:06:23	115	82	03:00:26	67	50	03:07:47
25-10-2013		83	74	13:37:05	68	61	13:38:47	152	139	13:37:14	128	113	13:38:50
08-11-2013		120	72	04:28:42	41	34	04:35:06	174	128	04:29:27	83	70	04:34:57
08-01-2014		84	76	03:51:12	43	37	03:56:21	174	145	03:50:40	88	77	03:55:45
11-02-2014		55	43	03:32:18	32	26	03:35:54	131	102	03:31:57	56	42	03:40:20
20-02-2014		60	52	03:22:37	45	40	03:25:37	118	102	03:22:34	93	79	03:25:25
20-02-2014		86	73	07:45:31	53	37	07:49:50	169	132	07:45:34	83	56	07:52:25
20-03-2014		48	39	04:01:18	35	31	04:05:18	98	80	04:00:50	69	58	04:06:00
01-08-2014		42	35	18:18:58	32	26	18:24:28	70	72	18:18:58	35	29	18:35:10
22-08-2014		121	102	00:09:14	91	78	00:10:44	176	146	00:09:50	102	92	00:13:40
25-08-2014		50	43	15:09:08	32	26	15:14:02	83	73	15:10:23	56	26	15:23:08
07-09-2014		82	70	02:04:20	62	52	02:06:25	180	151	02:03:10	84	73	02:08:50
23-09-2014		76	66	23:17:45	38	33	23:26:18	175	156	23:15:27	109	83	23:20:42
28-09-2014		91	84	02:46:02	50	45	02:53:09	171	138	02:46:20	97	85	02:53:42
02-10-2014		59	47	19:03:00	48	41	19:05:55	146	112	19:01:10	81	55	19:10:05
05-11-2014		167	126	09:43:56	52	42	09:52:00	175	137	09:46:44	75	60	09:56:17
07-11-2014		85	64	17:20:40	36	30	17:28:50	177	145	17:20:00	75	59	17:28:50
17-12-2014		42	32	04:44:00	31	25	04:48:15	67	52	04:46:33	36	26	05:01:12
20-12-2014		44	35	00:47:50	32	26	00:52:14	88	70	00:47:44	36	29	01:04:23
09-03-2015		92	77	23:42:10	51	43	23:52:55	177	140	23:42:35	103	78	23:52:40
21-12-2015		79	65	01:01:49	59	47	01:03:58	162	128	01:01:46	35	28	01:21:25
23-12-2015		67	56	00:36:10	31	25	00:41:45	130	98	00:36:20	36	26	00:48:39
02-05-2016		49	38	08:41:06	33	25	08:43:27	94	62	08:41:15	42	32	08:49:00
04-05-2016		57	43	13:55:22	41	33	13:58:19	83	71	13:57:25	41	35	14:09:30
10-07-2016		82	65	01:01:07	44	32	01:04:25	172	124	01:00:28	79	60	01:05:19
20-10-2017		88	70	23:30:05	41	33	23:38:30	172	127	23:30:10	84	62	23:37:20

Magdalenić, J., Marqué, C., Zhukov, A. N. et al. (2012). Flare-generated Type II Burst without Associated Coronal Mass Ejection. *Astrophys. J.*, 746(2), 152. doi:10.1088/0004-637X/746/2/152.

Magdalenić, J., Vršnak, B., Pohjolainen, S. et al. (2008). A Flare-Generated Shock during a Coronal Mass Ejection on 24 December 1996. *Solar Phys.*, 253(1-2), 305–317. doi:10.1007/s11207-008-9220-x.

Maguire, C. A., Carley, E. P., Zucca, P. et al. (2021). LOFAR Observations of a Jet-driven Piston Shock in the Low Solar Corona. *Astrophys. J.*, 909(1), 2. doi:10.3847/1538-4357/abda51.

Mahrous, A., Alielden, K., Vršnak, B. et al. (2018). Type II solar radio burst band-splitting: Measure of coronal magnetic field strength. *Journal of Atmospheric and Solar-Terrestrial Physics*, 172, 75–82. doi:10.1016/j.jastp.2018.03.018.

Mann, G., Classen, T., & Aurass, H. (1995). Characteristics of coronal shock waves and solar type II radio bursts. *Astron. Astrophys.*, 295, 775.

Mann, G., Klassen, A., Classen, H. T. et al. (1996). Catalogue of solar type II radio bursts observed from September 1990 to December 1993 and their statistical analysis. *Astron. Astrophys. Suppl.*, 119, 489–498.

Mann, G., Vocks, C., Warmuth, A. et al. (2022). Excitation of Langmuir waves at shocks and solar type II radio bursts. *Astron. Astrophys.*, 660, A71. doi:10.1051/0004-6361/202142201.

Michalek, G., Gopalswamy, N., & Xie, H. (2007). Width of Radio-Loud and Radio-Quiet CMEs. *Solar Phys.*, 246(2), 409–414. doi:10.1007/s11207-007-9062-y.

Morosan, D. E., Pomoell, J., Kumari, A. et al. (2023). A type II solar radio burst without a coronal mass ejection. *Astron. Astrophys.*, 675, A98. doi:10.1051/0004-6361/202245515.

Nelson, G. J., & Melrose, D. B. (1985). Type II bursts. In D. J. McLean, & N. R. Labrum (Eds.), *Solar Radiophysics: Studies of Emission from the Sun at Metre Wavelengths* (pp. 333–359).

Normo, S., Morosan, D. E., Zhang, P. et al. (2025). Imaging and spectropolarimetric observations of a band-split type II solar radio burst with LOFAR. *Astron. Astrophys.*, 698, A175. doi:10.1051/0004-6361/202553702.

Pikel'Ner, S. B., & Gintzburg, M. A. (1963). The Mechanism of Type II Bursts of Solar Radio Emission. *Astronomicheskii Zhurnal*, 40, 842.

Pohjolainen, S., Hori, K., & Sakurai, T. (2008). Radio Bursts Associated with Flare and Ejecta in the 13 July 2004 Event. *Solar Phys.*, 253(1-2), 291–303. doi:10.1007/s11207-008-9260-2.

Priest, E. R. (1982). *Solar magneto-hydrodynamics*. volume 21.

Reiner, M. J., Kaiser, M. L., Fainberg, J. et al. (1999). Remote radio tracking of CMEs in the solar corona and interplanetary medium. In S. R. Habbal, R. Esser, J. V. Hollweg, & P. A. Isenberg (Eds.), *Solar Wind Nine* (pp. 653–656). AIP volume 471 of *American Institute of Physics Conference Series*. doi:10.1063/1.58709.

Saito, K., Makita, M., Nishi, K. et al. (1970). A non-spherical axisymmetric model of the solar K corona of the minimum type. *Annals of the Tokyo Astronomical Observatory*, 12(2), 51–173.

Samwel, S. W., & Miteva, R. (2021). Catalogue of in situ observed solar energetic electrons from ACE/EPAM instrument. *Mon. Not. Roy. Astron. Soc.*, 505(4), 5212–5227. doi:10.1093/mnras/stab1564.

Sheeley, N. R., Jr., Howard, R. A., Michels, D. J. et al. (1985). Coronal mass ejections and interplanetary shocks. *J. Geophys. Res.*, 90(A1), 163–176. doi:10.1029/JA090iA01p00163.

Shen, J. M., Wu, G. P., & Zhu, Q. L. (2007). A Numerical study on the ion acceleration in the parallel shock wave. *Acta Astronomica Sinica*, 48(4), 433–440.

Smerd, S. F., Sheridan, K. V., & Stewart, R. T. (1974). On Split-Band Structure in Type II Radio Bursts from the Sun (presented by S.F. Smerd). In G. A. Newkirk (Ed.), *Coronal Disturbances* (p. 389). volume 57 of *IAU Symposium*.

Smerd, S. F., Sheridan, K. V., & Stewart, R. T. (1975). Split-Band Structure in Type II Radio Bursts from the Sun. *Astrophys. Lett.*, 16, 23.

Su, W., Cheng, X., Ding, M. D. et al. (2016). Investigating the Conditions of the Formation of a Type II Radio Burst on 2014 January 8. *Astrophys. J.*, 830(2), 70. doi:10.3847/0004-637X/830/2/70.

Thejappa, G., & MacDowall, R. J. (2000). Langmuir Waves in the Vicinity of interplanetary Shocks and the Consequences for Type II Burst Models. *Astrophys. J. Lett.*, 544(2), L163–L167. doi:10.1086/317303.

Tsap, Y. T., Isaeva, E. A., & Kopylova, Y. G. (2020). On the Evolution of Bands in the Dynamic Spectra of Solar Type II Radio Bursts. *Astronomy Letters*, 46(2), 144–148. doi:10.1134/S1063773720010053.

Umuhire, A. C., Gopalswamy, N., Uwamahoro, J. et al. (2021). Properties of High-Frequency Type II Radio Bursts and Their Relation to the Associated Coronal Mass Ejections. *Solar Phys.*, 296(1), 27. doi:10.1007/s11207-020-01743-8.

Vasantha, V., Umapathy, S., Vršnak, B. et al. (2014). Investigation of the Coronal Magnetic Field Using a Type II Solar Radio Burst. *Solar Phys.*, 289(1), 251–261. doi:10.1007/s11207-013-0318-4.

Vršnak, B., Aurass, H., Magdalenić, J. et al. (2001). Band-splitting of coronal and interplanetary type II bursts. I. Basic properties. *Astron. Astrophys.*, 377, 321–329. doi:10.1051/0004-6361:20011067.

Vršnak, B., Magdalenić, J., Aurass, H. et al. (2002). Band-splitting of coronal and interplanetary type II bursts. II. Coronal magnetic field and Alfvén velocity. *Astron. Astrophys.*, 396, 673–682. doi:10.1051/0004-6361:20021413.

Vršnak, B., Magdalenić, J., & Zlobec, P. (2004). Band-splitting of coronal and interplanetary type II bursts. III. Physical conditions in the upper corona and interplanetary space. *Astron. Astrophys.*, 413, 753–763. doi:10.1051/0004-6361:20034060.

Warmuth, A., & Mann, G. (2004). The Application of Radio Diagnostics to the Study of the Solar Drivers of Space Weather. In K. Scherer, H. Fichter, & B. Herber (Eds.), *Lecture Notes in Physics*. Berlin Springer Verlag (p. 49). volume 656. doi:10.1007/978-3-540-31534-6_3.

Warmuth, A., & Mann, G. (2005). A model of the Alfvén speed in the solar corona. *Astron. Astrophys.*, 435(3), 1123–1135. doi:10.1051/0004-6361:20042169.

Wild, J. P., & McCready, L. L. (1950). Observations of the Spectrum of High-Intensity Solar Radiation at Metre Wavelengths. I. The Apparatus and Spectral Types of Solar Burst Observed. *Australian Journal of Scientific Research A Physical Sciences*, 3, 387. doi:10.1071/CH9500387.

Zaitsev, V. V. (1977). Theory of solar type II and III radio bursts. *Radiofizika*, 20(9), 1379–1398.

Zaitsev, V. V. (1978). Theory of type II and type III solar radio bursts. *Radiophysics and Quantum Electronics*, 20(9), 951–965. doi:10.1007/BF01356766.

Zhang, X. J., Deng, L. H., Qiang, Z. P. et al. (2023). Hemispheric distribution of coronal mass ejections from 1996 to 2020. *Mon. Not. Roy. Astron. Soc.*, 520(3), 3923–3936. doi:10.1093/mnras/stad323.

Zimovets, I., Vilmer, N., Chian, A. C. L. et al. (2012). Spatially resolved observations of a split-band coronal type II radio burst. *Astron. Astrophys.*, 547, A6. doi:10.1051/0004-6361/201219454.

Zucca, P., Morosan, D. E., Rouillard, A. P. et al. (2018). Shock location and CME 3D reconstruction of a solar type II radio burst with LOFAR. *Astron. Astrophys.*, 615, A89. doi:10.1051/0004-6361/201732308.

Zucca, P., Pick, M., Démoulin, P. et al. (2014). Understanding Coronal Mass Ejections and Associated Shocks in the Solar Corona by Merging Multiwavelength Observations. *Astrophys. J.*, 795(1), 68. doi:10.1088/0004-637X/795/1/68.